PAPER

Check for updates

Study of heterogeneous chemistry and photochemistry of single sea-spray aerosols containing Hg(II) in air using optical trapping – Raman spectroscopy†

Yukai Ai, [ID] [a] Chuji Wang,*[a] Yong-Le Pan [ID] [b] and Gorden Videen[b]

Sea-spray aerosols (SSAs) contribute to atmospheric loading, bringing toxic compounds like mercury (Hg) to the atmosphere, affecting the climate and human health. Despite their importance, the investigation into surface modification, including heterogeneous chemical and photochemical reactions of SSAs, is limited. In this work, we studied the heterogeneous chemistry and photochemistry of a single suspended SSA particle and a SSA containing Hg(II) in a reactive environment using optical trapping – Raman spectroscopy. The experiments are focused on the study of hygroscopicity, heterogeneous chemical reaction with ozone (O_3), photochemical reaction with UVC radiation of an optically suspended single SSA particle, and photo-reduction of Hg(II) in SSAs under UVC radiation. Results show different Raman signal responses of a single SSA particle when it is optically trapped in air under varying relative humidity conditions as the aerosol particle uptakes and loses liquid water from the surrounding environment. The state and size of the aerosol are determined through the on-time images and different single-particle Raman spectral features. Results also show that the formation of chlorate (ClO_3^-) is a reaction product of the heterogeneous reaction between the SSA particle and O_3. The photochemical reaction products, as the SSA particle suspended in air under UVC radiation, are ClO_3^- and perchlorate (ClO_4^-). Further, we observed that these reactions occur only on the surface of the SSA particle. Based on the results, we hypothesize that Hg(II) can be photo-reduced to Hg(I) in SSAs through UVC radiation, and the amount of Hg(I) in SSAs is minor and balanced between the photo-oxidation and photo-reduction reactions.

Environmental significance

Sea-spray aerosols (SSAs) are an important component of atmospheric aerosols. The physical properties of SSAs, including hygroscopic properties, phase transitions, and component composition, have been well studied. However, the chemical temporal evolution, particularly surface modification, including heterogeneous chemical reactions and photochemical reactions, is less reported. This is a significant part of the aerosol's transmission in the atmosphere. Better understanding of their temporal evolution benefits actions on climate change, as well as disease control and prevention. We studied a single suspended SSA particle under a reactive environment using optical trapping, which simulates the behavior that might occur through a mitigation process of Hg(II). In particular, we studied the heterogeneous chemical reaction with O_3, the photochemical reaction with UVC light, and the photo-reduction of Hg(II) in SSA. This work casts new insights into our understanding of the chemical reactions that occur on the surface of SSAs and Hg(II)-contained SSAs in air and serves as a reference for subsequent studies.

1. Introduction

Sea spray is a dominant source of atmospheric aerosol loading formed in the marine boundary layer (MBL) and transmitted through wind and waves, influencing the climate, air quality, and human health.[1–3] Studies associated with the physical properties of a sea-spray aerosol (SSA), such as hygroscopic properties,[4–10] phase transition,[11–13] and component composition,[14–16] have been widely reported. However, the chemical reactions that occur on the surface of SSAs are less well studied. Sea spray is suspended in air and transmitted from the MBL to the atmosphere with gaseous reagents or air pollution surrounding it. The surface composition and properties of SSAs are subject to continuous change due to chemical reactions. For example, in the transmission process, SSAs react with air pollutants, such as SO_2, NO_2, and O_3. These reactions can change the chemical composition of the surface of SSAs.[16–18]

aDepartment of Physics and Astronomy, Mississippi State University, Starkville, MS, 39759, USA. E-mail: cw175@msstate.edu

bDEVCOM-U.S. Army Research Laboratory, 2800 Powder Mill Road, Adelphi, Maryland, 20783, USA

† Electronic supplementary information (ESI) available. See DOI: https://doi.org/10.1039/d4ea00053f

© 2024 The Author(s). Published by the Royal Society of Chemistry

Environ. Sci.: Atmos., 2024, **4**, 911–924 | **911**

Furthermore, SSA's surface properties are continuously influenced by solar radiation *via* photochemistry processes.[19] Without knowing the chemical composition changes or reactions that occur on the surface of SSAs, understanding the atmospheric behavior and environmental impacts of SSAs remains challenging.

SSAs are composed of a variety of inorganic and organic compounds.[14–16,20] Despite the complex composition, the major components are water and NaCl, which play significant roles in aerosol size, state, and morphology. Hygroscopicity is an important physical property of NaCl aerosol. A suspended aerosol particle in air continues to absorb or lose water from the ambient environment.[4,5] The amount of water that an aerosol particle contains is mainly determined by its environmental relative humidity (RH) which influences significantly the properties of the aerosol particle such as size.[8–10,21,22] When the RH decreases, the suspended SSA in air shrinks due to water evaporation and eventually crystallizes at a threshold RH value. This process is efflorescence, and the threshold RH value is termed efflorescence RH (ERH). The converse process is deliquescence, in which the solid aerosol particle starts to take up water from the surrounding environment as the RH reaches a high value. This RH value is termed deliquescence RH (DRH). The reported ERH of SSA is in the range of 35–47% depending on the composition and concentration of the solutes.[11,12,23–26] The DRH is typically 30% higher than the ERH. The reported DRH of SSA is 70–77%.[12,23–25] Normally, the SSA particle in air is in the liquid state when the environmental RH is higher than the ERH. However, if the surrounding RH of the SSA particle decreases from a high value to ERH, the solute in the liquid aerosol is supersaturated and the aerosol particle may be in an amorphous glassy state, with gel-like structures.[6,11] The changes in the water content subsequently affect the solute concentration in the aerosol.[27,28] In addition, the water content also impacts the aerosol's optical properties, *e.g.* scattering coefficient,[29,30] and refractive index.[31] On the other hand, variations in the solute concentration change the pH value of the aerosol.[32] Furthermore, the RH affects directly the chemical reactions that happen on the aerosol's surface. Several studies have reported that the RH affects the heterogeneous chemical reactions that happen on the surface in the formation and evolution of secondary organic and inorganic aerosols in air.[33–37]

The other major component of SSA is NaCl. The ionic Cl in aqueous droplets can be oxidized to chlorate (ClO_3^-) and perchlorate (ClO_4^-), which are extremely toxic to humans. It was reported that Cl^- can be oxidized by O_3 in the natural environment.[38–40] The reaction of O_3 with Cl^- in aqueous solution was first reported by Yeatts *et al.*[41] The results showed that the reaction can be catalysed by H^+ ions. Kang *et al.* reported that ClO_4^- can be formed *via* homogeneous photochemical reactions of aqueous oxychloride precursors.[42] Later on, they reported a number of potential reaction mechanisms of ClO_3^- and ClO_4^- production in the natural environment through the oxidation of Cl^- by O_3.[38] However, the reactions observed in the references mentioned above are measured from bulk solutions, where the heterogenous reaction between Cl^- and O_3 can only happen on the interface between air and solution. Therefore,

the reaction is extremely slow. Different from the bulk solutions, NaCl aerosols suspended in air are on the order of micrometer in size with a high surface-to-volume ratio, which provides sufficient surface area for interactions with gaseous phase atoms and molecules, so the O_3 can rapidly overwhelm the suspended droplet. In this case, the oxidation reaction that occurs on the surface of SSAs in the atmosphere would be rapid.

In addition to water and NaCl, toxic substances that SSAs carry, including mercury (Hg), are transmitted from the MBL to terrestrial environments.[43,44] This toxic compound can directly cause serious impacts on the environment and humans. The ocean is a significant reservoir for Hg. It is estimated that ocean waters contain 3.5×10^8 kg of Hg.[45] The Hg from ocean emissions to the atmosphere is estimated at 2.68×10^6 kg per year, which contributes approximately 40% of the total Hg input.[46,47] A significant amount of Hg that exists in SSAs is transmitted to terrestrial environments. Holmes *et al.* used a chemical box model to predict that about 85% of Hg is partitioned into SSAs under typical MBL conditions.[48] Moreover, the Hg concentration in SSAs is suggested to be higher than that found in seawater. Malcolm *et al.* reported that the Hg concentrations in SSAs can be up to 3000 times greater than in the marine system if seawater is the only source of the Hg to the aerosols.[49] In this case, a complete understanding of atmospheric mercury's chemical reactions and physical transformations that happened on the surface of SSAs is crucial to predicting mercury emissions.

Hg exists in the atmosphere in three different forms: elemental gaseous Hg (EGM or Hg(0)), reactive gaseous Hg (RGM or Hg(II)), and particulate bond Hg (PBM or Hg(p)).[50,51] As most Hg(II) compounds are water-soluble, the Hg in SSAs is primarily Hg(II), with the majority being $HgCl_2$. In the process of transmission of SSAs, the state of Hg(II) in the aqueous droplets will be affected by the surrounding environment. For example, SSAs contribute most RGM and PBM in the atmosphere in terms of the evaporation of Hg(II) compounds to the air and deposition of these species on the surface of aerosols.[52] Then, the RGM or PBM may further be reduced to Hg(0) under the specific condition.[47,50,51] The GEOS-Chem global model has postulated that Hg(II) photoreduction that occurs on the aqueous droplets in the atmosphere takes place in tropospheric clouds.[52–54] Malcolm *et al.* reported that SSAs could scavenge the RGM and significantly reduce Hg(II) levels in the air.[49] Tong *et al.* demonstrated that Hg(II) can be photolyzed to Hg(0) on the surface of NaCl aerosols under solar radiation.[55] Hedgecock *et al.* modeled the SSA effects on the photoreduction of Hg(II) and reported that the effect of the SSA is more related to the scavenging and deposition of Hg(II) than the catalytic reduction from Hg(II) to Hg(0).[56] Many researchers have reported the redox reaction of Hg(II) and Hg(0) in the aquatic system.[57–60] However, all results from the references mentioned above are only known from computations or have been measured and tested experimentally from bulk systems (ocean and bulk aqueous solution). The reduction or photodissociation mechanisms of Hg(II) in the atmosphere remain uncertain. Due to the lack of understanding of the chemical-reaction mechanism of this process, the model

cannot provide an accurate description of the global mercury distribution.

To date, most atmospheric studies conducted in field or lab focused mainly on the composition and properties of freshly emitted SSA or SSA simulants.[61] However, atmospheric aging processes can transform SSA through reactions with trace gases, air pollutants, oxidants, and solar radiation.[61–67] Many SSA's atmospheric behaviors, such as the heterogenous chemical reaction on aerosol modification,[62–64] the production of volatile organic compounds,[61,65] the formation of secondary organic aerosols (SOA),[65] and the formation of secondary marine aerosols (SMA)[66,67] *etc.*, have not been well studied. This is mainly because of experimental difficulties in analyzing aerosols directly. For example, in current lab experiments, it is extremely challenging to accurately control the biological and chemical processes that lead to the formation of the SOA or SMA.[65–67] In the traditional method of aerosol characterization, measurements are made from the collected samples deposited on substrates, offering only information from the bulk materials. Furthermore, because of offline measurement, important information like the actual atmospheric behavior, such as changes in surface composition due to reactions and equilibrium processes, is missing. Another approach is to consider flowing aerosols in a tube or a reaction chamber. However, the aerosol particles will inevitably be affected by wall effects. To avoid these interferences and better understand the behavior of the aerosol in the atmosphere, investigation at the single-particle scale is of significance. Numerous studies that focus on the hygroscopic properties of single, suspended salt aerosols based on different techniques, including optical trapping (OT) and through an electrodynamic balance, have been reported.[4–8,13,22] These works only focus on physical properties, *e.g.*, phase transition, of the aerosols. No surface-composition changes and chemical reactions of SSAs at the single-particle scale have been reported. However, this missing part is crucial for understanding SSA's influence on atmospheric processes and human health.

In this work, we study the heterogeneous chemistry and photochemistry of a single, suspended SSA particle and SSA containing Hg(ɪɪ) in a reactive atmospheric environment using optical trapping – Raman spectroscopy (OT-RS). This paper consists of two parts. Part I studies the heterogeneous chemistry and photochemistry of the optically trapped single SSA particle, and Part II considers the photo-reduction reaction of Hg(ɪɪ) in SSA. The major objectives of this two-part study are: (1) through the size and spectral evolution of an SSA particle trapped under different RH conditions, we estimate the size of the aerosol particle using different Raman signal features. (2) By investigating the heterogeneous chemical reaction with O_3 and the photochemical reaction with UVC radiation of the SSA particle, we show that the ionic Cl in the SSA can be oxidized to chlorate (ClO_3^-) by O_3 and further oxidized to perchlorate (ClO_4^-) by UVC radiation, and that these reactions occur only on the surface of SSA. (3) *Via* the study of the photochemical reaction of Hg(ɪɪ) in SSA particles with UVC radiation, we shed insight on the photo-reduction and photo-oxidation reactions between Hg(ɪɪ) and Hg(ɪ) in the SSA. This study from the single particle

provides unique insight into the connections between atmospheric chemistry and aerosol properties and demonstrates how OT-RS can be used to isolate and study reactions of the single particle in a reactive environment in the laboratory under controlled conditions. This work will be a reference for subsequent research work that applies to real atmospheric environmental conditions in the future.

2. Methodology

2.1 Experimental setup

Fig. 1 is the schematic of the experimental system. The details of the experimental setup of OT-RS can be found in our previous publications[68–70] and are briefly described here. A 532 nm (TEM_{00}) continuous Gaussian laser beam is used as the trapping laser beam. The laser power is set at 1740 mW in this experiment to trap all the droplet particles. A beam splitter splits the trapping laser beam into two perpendicular beams of equal intensity. These two beams pass through axicons to form hollow beams. The universal optical trap is formed in the overlapping region of these two counter-propagating hollow beams through two micro-objectives ($\times 50$, numerical aperture (NA) = 0.55) as shown in Fig. 1. The size of the optical trap can be varied from $\sim$10 μm to 100 μm by tuning the position of the two micro-objectives. The scattering signal from a trapped droplet particle can be collected through another micro-objective ($\times 20$, NA = 0.42). The collected information passes through a dichroic beamsplitter. The short passing beam is delivered to a camera to show the trapped particle's physical information, such as size, shape, and position. The long passing beam is directed to a spectrograph (Acton 2300i, Princeton) that shows the inelastic scattering signal containing the chemical properties, *e.g.*, the vibrational band information. The Raman information is dispersed by a 600 lines per mm grating and then projected onto an electromagnetic charge-coupled device (EMCCD, ProEM, Princeton), which has a spectral resolution of 0.05 nm per pixel. With the experimental setup in this work, the best spatial resolution that can be achieved is 600 nm × 600 nm.[71] The integration time of spectra is set to 60 s, and the spectrograph slit is set to 100 μm.

The aerosol particle is generated through a humidity diffuser and introduced directly into the chamber. A light is installed on the side of the chamber to illuminate the trapped particle. Ozone is generated through a homemade ozone generator and introduced through the same hole as the humidity diffuser after introducing the aerosol particles. At the bottom of the chamber, a hole is connected to a mechanical pump, which is controlled by a valve at a slow pumping rate of 0.01 L min^{-1}. The ozone flows through the trapped droplet and then is pumped out through the bottom hole. The ozone flow is also set at a low rate of 0.01 to 0.2 L min^{-1}. The pressure and RH around the trapped droplets are not affected as both the pumping and flowing rates are slow. The RH and temperature sensor are fixed inside the chamber to monitor the local conditions. In addition to the hole on the bottom, which is connected to a valve, the top hole of the chamber is open during the experiment, so the pressure and temperature (19–21 °C) inside the chamber are the same as in

© 2024 The Author(s). Published by the Royal Society of Chemistry

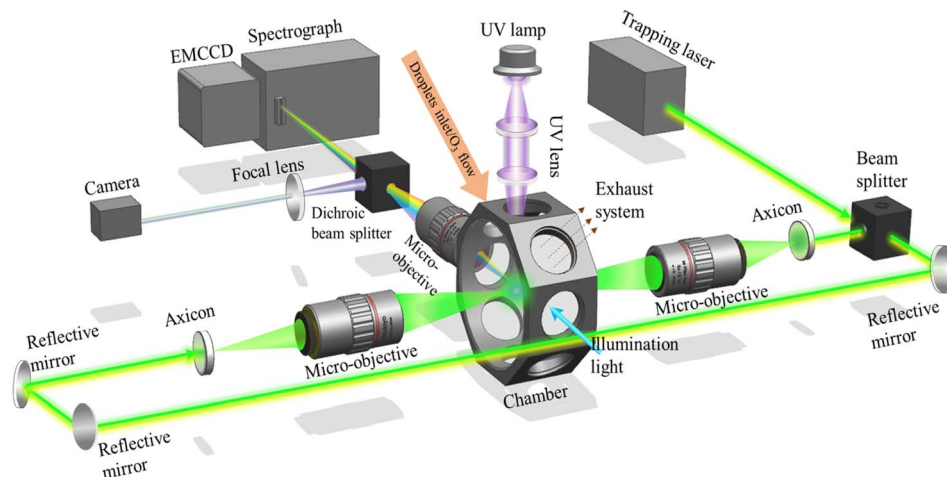*Environ. Sci.: Atmos.*, 2024, **4**, 911–924 | **913**

Fig. 1 Schematic of the experimental setup of the OT-RS system.

the lab environment. The humidity diffuser keeps generating droplet aerosols for 30 to 60 seconds until one droplet is stably trapped. As the chamber is not sealed, most of the excessive mist will be pumped out through the bottom hole, and the few leftovers pass out of the chamber through the open hole to the exhaust system. In the experiment, two RH sensors are installed, one installed inside of the chamber, and another installed outside of the chamber. The sensor inside the chamber shows increase of RH when introducing the droplets aerosol, and decrease of RH when the aerosol introduction is stopped. Finally, after the aerosol particle is trapped for several minutes, the RH shown by the two sensors becomes the same. In this case, after several minutes of stopping aerosol particle introduction, the RH around the trapped particle is consistent with the laboratory RH. The recorded RH in the lab for the whole year is in the range of 30–70%. For the extremely high RH cases (RH > 70%), an external humidifier is connected to maintain the high RH condition inside the chamber. The UVC radiation is generated from a UV lamp (90-0049-01/ Photochemical Lamps, Analytik Jena US), which is fixed on the top area of the chamber. Two wavelengths can be generated, 254 nm (>95%) and 185 nm (<5%), both of which are in the UVC region, with an irradiance intensity of 4000 μW cm^{-2}. The UVC radiation is focused into the chamber through two UV lenses. Counting the distance of 2.5 cm between the first lens and UV lamp, and the maximum energy loss of 20% at 254 nm of the two lenses, the irradiance applied on the trapping area is calculated as 512 μW cm^{-2}.

2.2 Samples

The droplets are produced by ultrasonic nebulization through a humidity diffuser of aqueous solutions. SSA particles used in this work were SSA simulants generated from the 3.5% NaCl solution. The solution to generate droplets of SSA containing Hg(II) is made by adding 1% HgCl$_2$ into 3.5% NaCl solution. The NaCl (>99.5%) was purchased from Fisher Scientific, and the HgCl$_2$ (>99.5%) was purchased from Sigma-Aldrich.

3.   Results and discussion

3.1   Part I: the study of heterogeneous chemistry and photochemistry of the optically trapped single SSA

3.1.1   Effects of surrounding RH on size and Raman spectral features of an SSA particle. In the experiment, the trapped droplet continues to uptake or lose water from the ambient environment during the trapping period. Fig. 2a shows the Raman spectrum of the droplet trapped in a dry environment with a RH of 37%. The Raman bands and band assignments are shown in Table S1.† Three Raman bands at 185 cm^{-1}, 1630 cm^{-1}, and 3430 cm^{-1} are observed and assigned to O–H$\cdots$O stretching mode, OH-bending mode, and OH-stretching mode of water, respectively. The spectrum of Fig. 2a is from an aerosol particle trapped under RH of 37%. Under this dry condition, the OH stretching mode is extremely weak. This is because the trapped NaCl aerosol particle experiences efflorescence, and the solute becomes supersaturated.[11] In this experiment, the ERH we calculated is 39% ± 8%, which is consistent with the reported results.[11,12,23–26] This value was obtained from 20 sets of data in which the Raman signals have no or very weak OH-stretching band. Therefore, the dry and wet conditions in this experiment is defined as when the RH are below and above 39% ± 8%, respectively. The size of the inset image is 500 pixels × 500 pixels, corresponding to approximately 83.3 μm × 83.3 μm, which was used to estimate size of each droplet shown in Fig. 2. For instance, the size of the trapped droplet in Fig. 2a is 4.4 μm. If the RH further decreases, the SSA undergoes efflorescence and crystallization, forming a solid particle.[11] Fig. 2b shows the Raman spectrum of the SSA trapped in air with a RH of 55%. Different from Fig. 2a, a wide and strong Raman band of OH-stretching located around 3430 cm^{-1} is observed. This indicates that the droplet is in the aqueous state. Thus, the NaCl inside the droplet is in the ionic state. The size of the droplet shown in the on-time image in Fig. 2b was estimated to be 9.3 μm under this RH condition. Because the amount of water a particle can absorb is affected by the surrounding RH, therefore, under different RH conditions,
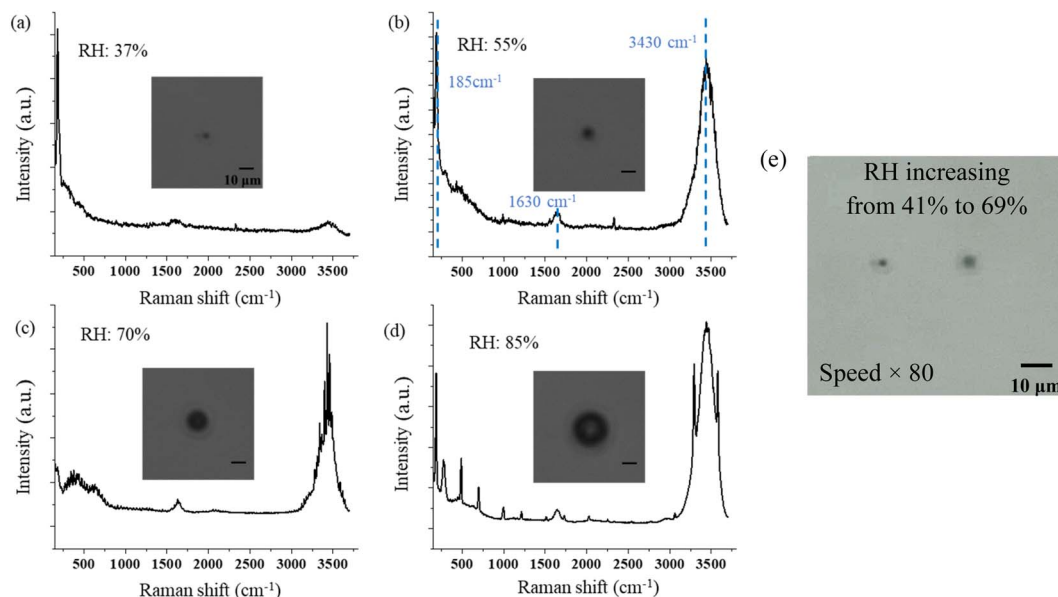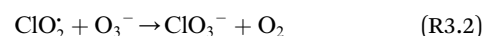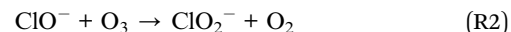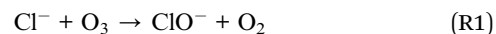
Fig. 2 (a–d) Single-particle Raman spectra of the SSA particle trapped in air under different RH. The inset pictures are the on-time images corresponding to the Raman spectra, captured by the system camera. (e) A video showing the SSA particle's size evolution as the surrounding RH increases from 41% to 69%.

the intensity of the OH band is different. As shown in Fig. S1,† the intensity of the Raman signal changes as the surrounding RH changes. The on-time images, which show the size of the droplets corresponding to different RH, are shown in the insets of Fig. S1a.† The Raman signal intensity is increasing or decreasing with the changing of the size of the SSAs. Fig. S1b† shows the relationship between the intensity of Raman band at 3430 cm^{-1} and the size of the trapped droplet. The result shows that the Raman band intensity is linear to the particle size, which implies that the size of the SSAs can be estimated using the Raman spectral features. Further increasing RH would increase the water content of the aqueous droplet, *i.e.*, the aqueous particle would become more diluted,[11] and the size of the droplets would also increase simultaneously. When the trapped droplets reach a specific size, the whisper gallery mode (WGM) can be observed from the Raman spectrum.[72] In the experiment, as the surrounding RH is above 69% ± 5% (similarly, this number was obtained from 20 sets of data), the WGM can be observed. Fig. 2c and d show the WGM in the Raman spectra of the NaCl droplet trapped in air with RH of 70% and 85%. The size of the droplets in these two cases are 18.5 μm and 27.8 μm, respectively. Fig. 2e is a snapshot from a video that shows the size evolution as the SSA particle trapped in air with the surrounding RH increases from 41% to 69%. The video's playing speed has been accelerated by 80 times; this whole process lasts about 22 minutes in the experiment.

3.1.2 The heterogeneous chemical reaction between O₃ and Cl⁻ in a single SSA particle. Fig. 3 shows the time-resolved Raman spectra of a trapped SSA particle exposed to ozone at a RH of 62%. The ozone concentration used in this experiment is 1000 ppm. In the experiment, the O_3 concentration is measured in an independent chamber on the way of O_3 flowing.

So the measured O_3 concentration is a direct result from the ozone generator. The O_3 flows into the chamber and through the trapped aerosol particle. The O_3 concentration is much diluted in the chamber as the flowing rate is very low, and the chamber is opened to air, so that the air inside and outside the chamber is constantly being exchanged. But compared with the volume of the trap, the covered area of O_3 flow is much larger. In this case, 1000 ppm is an upper limit of O_3 concentration involved in the reaction. In Fig. 3, one peak appears and increases slowly with time after the droplet is trapped in the ozone environment for 20 minutes. This peak is located at 966 cm^{-1} and attributed to ClO_3^-. The ClO_3^- is generated through oxidation of the ionic Cl in the aqueous solution by O_3.[17,38,39,73,74] The reactions are as follows from (R1) to (R3.2).

$$Cl^- + O_3 \rightarrow ClO^- + O_2 \tag{R1}$$

$$ClO^- + O_3 \rightarrow ClO_2^- + O_2 \tag{R2}$$

$$ClO_2^- + O_3 \rightarrow ClO_2^{\cdot} + O_3^- \tag{R3.1}$$

$$ClO_2^{\cdot} + O_3^- \rightarrow ClO_3^- + O_2 \tag{R3.2}$$

$$ClO^- + O_3 \rightarrow Cl^- + 2O_2 \tag{R4}$$

However, ClO^- also can be reduced to Cl^- through (R4). The reaction rates $k_1 = 3 \times 10^{-3} \text{ M}^{-1} \text{ s}^{-1}$ and $k_2 = 30 \text{ M}^{-1} \text{ s}^{-1}$ are much smaller than $k_4 = 110 \text{ M}^{-1} \text{ s}^{-1}$ at room temperature around 20 °C.[38,75] Therefore, the production of ClO_3^- is very limited. However, these reaction rates were measured from a bulk aqueous solution, in which the reaction happens only on the interface between the liquid solution and air.[76] Compared
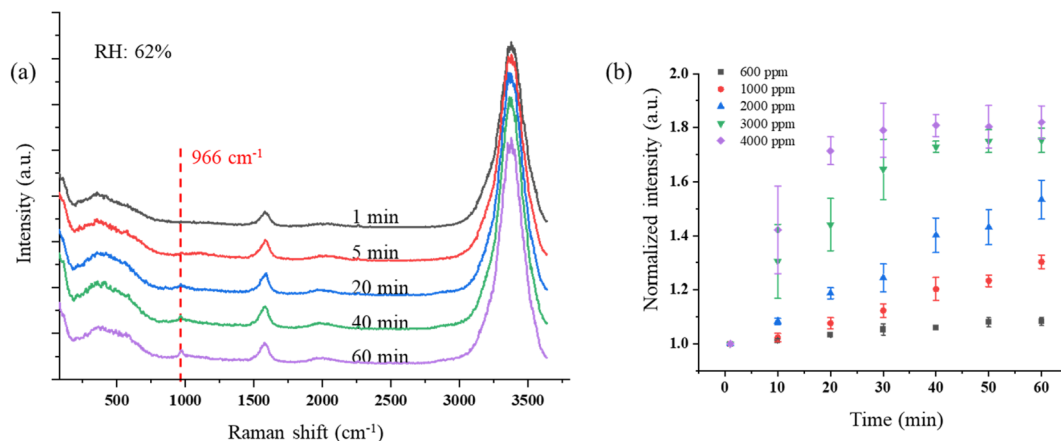
© 2024 The Author(s). Published by the Royal Society of Chemistry

Environ. Sci.: Atmos., 2024, **4**, 911–924 | **915**

Fig. 3 (a) The time-resolved Raman spectra indicate the formation of ClO_3^- as the SSA particle is exposed to O_3 at 1000 ppm and RH of 62%. (b) Time variations of the intensity of the Raman band of ClO_3^- at 966 cm^{-1} as the single trapped SSA particle is exposed to different O_3 concentrations.

with the reaction that happens only on the interface, ozone can soon overwhelm the droplet particle as it is suspended in air because of the high surface-to-volume ratio, which greatly accelerates the reaction. Fig. 3b shows the peak intensity of 966 cm^{-1} increasing as the droplets are trapped in different O_3 concentrations with the RH of 54–62%. Each data point in Fig. 3b was averaged over three points and normalized to the first minute's peak intensity. In Fig. 3b, the Raman band of ClO_3^- increases slowly with the peak intensity at a rate of 0.0015 minute^{-1} when the trapped droplets are exposed to O_3 at 600 ppm. The reaction becomes faster with increasing ozone concentration. As shown in Fig. 3b, the intensity increases at a rate up to 0.027 minute^{-1}, 18 times faster, as the O_3 concentration increases to 4000 ppm. After the reaction is completed within 30 minutes, the band intensity still increases slightly. This is because that the reaction happens only on the surface of the suspended droplet (details shown in Section 3.1.3). As the ion exchanges between the surface and the interior consistently happen in the aqueous system after all the Cl$^-$ has been oxidized on the surface, the supplied Cl$^-$ continually reacts with ozone and produces ClO_3^-.

No change in the Raman bands is observed when the ozone concentration is below 600 ppm. This is because the concentration of ClO_3^- is too low to be observed in the first several hours. Furthermore, since (R4) is much faster than (R1), with low O_3 concentrations, the ClO$^-$ is produced at a lower rate and balanced with Cl$^-$ in the aqueous system of the droplet, and no further reaction of (R2) and (R3) happens. Therefore, there will be less ClO_3^- produced. Nevertheless, even though the reaction is faster in the suspended droplets than in bulk solution, with the low concentration of O_3 in air, this reaction is still slow in the natural environment. On the other hand, this reaction was observed only at the environmental RH of 39–69%. Experimentally, due to the loss of water, the solute in the suspended NaCl aerosol particle becomes supersaturated in the dry environment when the surrounding RH is lower than 39% $\pm$ 8%. Under this condition, the ionic Na and Cl are bounded to form

NaCl molecules. Therefore, the amount of Cl$^-$ on the surface of the droplet is not sufficient to produce enough ClO_3^- that is observable.

Compared with the reported Raman band position of v_1 (ClO_3^-), which is located around 940 cm^{-1},[77,78] the Raman band position in this study is blue-shifted to 966 cm^{-1}. This may be caused by a change in the Cl–O band frequency due to the adsorbate and adsorbent interaction, which is absent in the bulk liquid state.[79,80] Furthermore, the concentration of NaCl also affects the force of the Cl–O band, affecting the vibrational frequency. Zachhuber *et al.* reported that the Raman band of v_1 (ClO_3^-) of a mixture of 50% NaCl and 50% NaClO$_3$ shifted to 998 cm^{-1}.[81] Additionally, changes in PH value and temperature in the aqueous environment as a result of laser heating can also slightly change the Raman band position of ClO_3^-. All the factors above are possibly attributed to the blue-shifting of the Raman band of ClO_3^- observed in this result.

3.1.3 The photochemical reaction of single suspended SSA particle with UVC radiation. Time-resolved Raman spectra of a SSA exposed to UVC of 185 nm and 245 nm radiation are shown in Fig. 4. The surrounding RH of the trapped droplet is
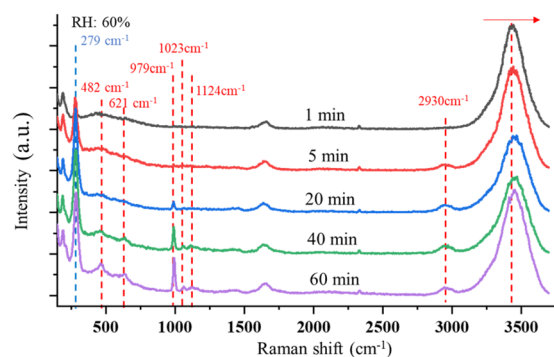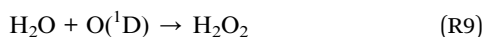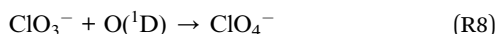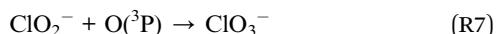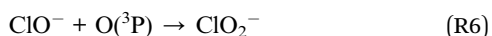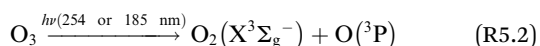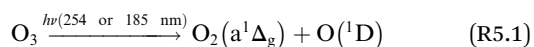

Fig. 4 Changes in the time-resolved Raman spectra indicate the formation of ClO_3^- and ClO_4^- as the SSA particle is trapped under UVC radiation with RH of 60%.

© 2024 The Author(s). Published by the Royal Society of Chemistry

60%. The Raman band assignments corresponding to Fig. 4 are shown in Table S1.† Compared with the Raman spectra of the aerosol droplet trapped in the first minute, five more Raman bands were observed after exposure to the UVC radiation. Among them, four bands at 482 cm^{-1}, 621 cm^{-1}, 979 cm^{-1}, and 1023 cm^{-1} are attributed to ClO_3^-, and one weak band located at 1124 cm^{-1} is assigned to ClO_4^-. Different from the SSAs exposed to O_3, the Raman band of v_1 (ClO_3^-) at 966 cm^{-1} shifts to 979 cm^{-1}. As discussed in the previous section, this can be explained by the adsorbate and adsorbent interaction in the single-particle scale and the changes in concentration of the Cl^- and ClO_3^- inside the droplet. Nevertheless, the intensity of v_1 (ClO_3^-) became much stronger, and more Raman bands related to ClO_3^- were observed, which indicates that more oxidated product of ClO_3^- was produced due to the UVC radiation than that in the condition of the droplets exposed to ozone. Note that the vibration frequency of v_3 (ClO_3^-), which is reported to be 976 cm^{-1} (ref. 82 and 83) blue-shifts to 1023 cm^{-1}, but the frequency difference between v_1 (ClO_3^-) and v_3 (ClO_3^-) is the same as reported.[82,83] As v_1 (ClO_3^-) and v_3 (ClO_3^-) are from the stretching vibration, these two bands show consistent frequency shifts, while the bending bands of v_2 (ClO_3^-) and v_4 (ClO_3^-) retain the same frequency as reported.[82,83]

In this reaction, UVC radiation photolyzes oxygen to produce ozone around the trapped droplets, and O_3 reacts with the ionic Cl on the surface of the droplets to produce ClO^-, which is the same as (R1) in Section 3.1.2. Additionally, due to the reaction product of O(^3P) and O(^1D) from the photolysis of O_3,[84] more chemical reaction pathways can exist, which lead to further production of ClO_3^-, e.g., via reactions (R5)–(R7) below.[40,42] This explains the much stronger Raman band of ClO_3^- observed.

$$O_3 \xrightarrow{h\nu(254\ or\ 185\ nm)} O_2(a^1\Delta_g) + O(^1D) \tag{R5.1}$$

$$O_3 \xrightarrow{h\nu(254\ or\ 185\ nm)} O_2(X^3\Sigma_g^-) + O(^3P) \tag{R5.2}$$

$$ClO^- + O(^3P) \rightarrow ClO_2^- \tag{R6}$$

$$ClO_2^- + O(^3P) \rightarrow ClO_3^- \tag{R7}$$

$$ClO_3^- + O(^1D) \rightarrow ClO_4^- \tag{R8}$$

$$H_2O + O(^1D) \rightarrow H_2O_2 \tag{R9}$$

One Raman band that is attributed to ClO_4^- was also observed. This indicates ClO_3^- is further oxidized by O(^1D) to ClO_4^- via (R8). In addition to the Raman band related to ClO_3^- and ClO_4^-, a wide Raman band located in the range 2900–2960 cm^{-1} appears and rises slowly as the particle is trapped. This wide band indicates the formation of H_2O_2.[85] The H_2O_2 formation is due to the reaction between O(^1D) and H_2O (R9). The detailed reaction pathways can be found in ref. 86 and 87, while the major reaction is (R9).

In addition to the new Raman bands of ClO_3^- and ClO_4^-, it is important to notice the changes in the OH-stretching band. Compared with the spectra in the first minute and after 60 minutes, the center of the band moves from 3430 cm^{-1} to

3450 cm^{-1}. This is mainly due to the Cl^- being oxidized to ClO_3^- and ClO_4^-.[88] However, this happens only on the surface of the trapped droplets. Fig. 5 shows a contour plot of the Raman spectrum intensity distribution of the SSA trapped under UVC radiation for 60 minutes. Two places marked as S and C correspond to the surface and center of the trapped droplet, and the image shows the position of these two locations. The inset also shows the Raman spectra of the OH-stretching from these two locations. The maximum intensity of the two Raman spectra is normalized to be the same. Comparing the spectra from these two locations, the Raman band of OH-stretching is located at 3430 cm^{-1} in position C, while it moves to 3450 cm^{-1} in position S. This suggests that the ion distribution is also different between the surface and the center of the trapped droplet. In particular, more ClO_3^- is located on the surface of the droplet, and more Cl^- is in the center. This suggests the reaction between Cl^- and O_3 happened only on the surface of the droplet.

Fig. 6 shows the time-resolved Raman spectra of a single SSA particle exposed to UVC radiation and trapped in a dry environment with the RH of 38%. The intensity of the OH-stretching band around 3400 cm^{-1} becomes weaker under this condition. The Raman spectra show only one new Raman band rising as the droplets are exposed to UVC radiation under this dry condition, which is located at 2930 cm^{-1}. This band indicates the formation of H_2O_2. No other band change was observed during this process. Therefore, different from the SSA trapped in a higher RH environment, no oxidation reaction of Cl^- was observed. This also suggests that the reaction between Cl^- and O_3 occurs only when the environmental RH is relatively high. As discussed in Section 3.1.2, the solute in the suspended droplet becomes saturated in a dry environment, and ionic Cl is in the state of NaCl rather than free Cl^- in the aqueous system. In this case, without enough Cl^- appearing on the surface of the suspended droplets, the oxidation reaction with O_3 becomes less likely; thus, the reaction product of ClO_3^- is hard to observe.

Under the UVC radiation, the Cl^- on the surface of the droplets is oxidized to ClO_3^- when the single SSA particle is trapped in air with a high RH condition. The reaction is much faster than that of a single SSA particle exposed to ozone at
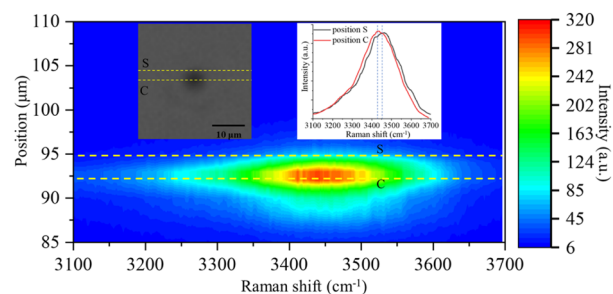

Fig. 5 Contour plot of the spectral intensity distribution of the OH-stretching mode for Raman spectra of SSA. Two places are marked where S is the surface and C is the center. The inset picture shows the on-time image captured by the system camera; the inset figure shows the position-resolved Raman spectra from the two marked locations.
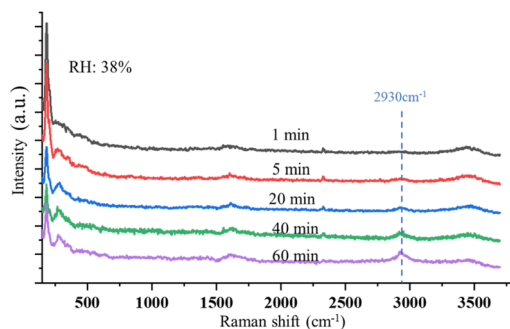
© 2024 The Author(s). Published by the Royal Society of Chemistry

Environ. Sci.: Atmos., 2024, 4, 911–924 | 917

Fig. 6 Time-resolved Raman spectra of a single, suspended SSA particle is exposed to UVC radiation with RH of 38%. No Raman band changes occur except for the peak at 2930 cm^{-1} appearing.

4000 ppm, even though (R1) is the same for both oxidation pathways. This is mainly because the atomic O that is photolyzed from O_3 enhances this process *via* additional reactions of (R5)–(R7). The same oxidation reaction also can occur on the surface of a SSA in the atmosphere. While the high concentration of O_3 and UVC radiation are not reflective of the natural atmosphere, the experiment does confirm oxidation pathways suggested previously.[38–41]

3.2 Part II: the study of heterogeneous chemical reactions and photochemistry of a single SSA containing Hg(II)

3.2.1 Effects of surrounding RH on size and Raman spectral features of a SSA containing Hg(II). Fig. 7 shows the Raman spectra of a SSA particle containing Hg(II) trapped in air under different RH conditions. Fig. 7a shows the Raman spectra of the droplet trapped in a dry environment with a RH of 39%. One more Raman band, compared with pure SSA, located at 314 cm^{-1}, is observed, which is attributed to $HgCl_2$.[89] As discussed in Section 3.1.1, the droplets do not crystallize, but the solute in the aqueous system becomes supersaturated when the surrounding RH is low. In this case, part of the free Hg^{2+} inside

the aqueous droplets is bound to Cl^- to form $HgCl_2$ molecules in an aqueous system. So, the Raman signal of the $HgCl_2$ band can be observed. With different RH, the band of $HgCl_2$ shows different intensities, indicating an increase or decrease in the amount of $HgCl_2$ molecules. The related figures are shown in Fig. S2.† In the experiment, the ERH for SSA containing Hg(II) is calculated to be 41% ± 11%. This value is calculated through 20 data sets in which the Raman signals show the Raman band of $HgCl_2$. Due to the $HgCl_2$ added, the ERH of SSA containing Hg(II) is slightly higher than the pure SSA. When the RH increases above the ERH of SSA containing Hg(II), as shown in Fig. 7b, the $HgCl_2$ vibration band at 314 cm^{-1} disappears, and the Raman signal of the OH-stretching band around 3400 cm^{-1} is observed. This indicates that Hg(II) turns to the ionic state in the aqueous system under the higher RH condition. The changes in size are similar to the pure SSA as discussed in Section 3.1.1, which indicates that the hygroscopicity of SSA particles is not affected by the Hg(II) contained in the droplet.

3.2.2 The heterogeneous chemical reaction between SSA containing Hg(II) and O_3. The time-resolved Raman spectra of the droplets of SSA containing Hg(II) exposed to O_3 are shown in Fig. S3.† The O_3 concentration is 1000 ppm. Fig. S3a† shows the single droplet trapped in an O_3 environment with a surrounding RH of 58%. This figure is similar to the pure SSA in Fig. 3 with one peak located at 966 cm^{-1}, which is attributed to ClO_3^- that increases slowly with time. The peak intensity increases with the increase of the O_3 concentration, and the rate is also similar to the results in Fig. 3b of pure SSA. Fig. S3b† shows the SSA containing Hg(II) exposed to O_3 of 1000 ppm in a RH of 35%. As mentioned in Section 3.2.1, when the RH is below the ERH of 41% ± 11%, the solute in the droplets becomes saturated, and the peak at 314 cm^{-1} of $HgCl_2$ is observed. In Fig. S3b,† the peak at 314 cm^{-1} is observed in the first minute and kept steady for the rest of the trapping time. In this case, the reaction mechanism of the SSA containing Hg(II) is the same as the pure SSA with the reaction product ClO_3^- when the RH is above the ERH of SSA containing Hg(II). No reaction between O_3 and $HgCl_2$ was
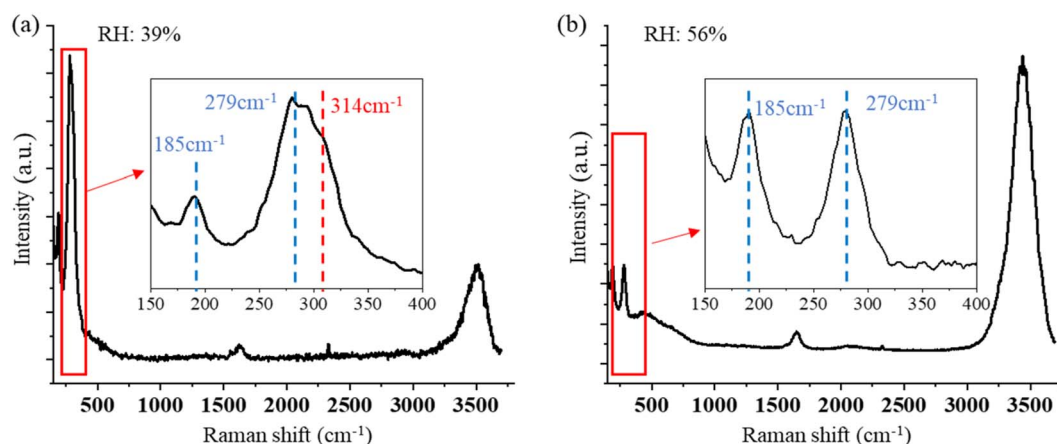

Fig. 7 Sigle-particle Raman spectra of the SSA containing Hg(II) trapped in air under different RH. The inset figure shows the Raman spectra with high resolution in the region of 150–400 cm^{-1}. The Raman band of $HgCl_2$ at 314 cm^{-1} can only be resolved as the SSA particle is trapped in a dry environment with RH below 41% ± 11%.

observed. This result indicates that the HgCl$_2$ molecule in the suspended droplet is stable when the SSA particle is exposed to O$_3$.

3.2.3 The photochemical reaction of Hg(II) in SSA under UVC radiation.

The Raman spectra of a SSA containing Hg(II) trapped with RH of 56% exposed to UVC radiation are shown in Fig. S4.† The spectra show similar changes to those in Fig. 4, which indicates the reaction products are similar to those of the pure SSA. However, compared to Fig. 4, a blue-shift in the vibrational band of OH-stretching at 3457 cm^{-1} is observed, as shown in Fig. S4.† This difference could be caused by the stronger ionic force as the concentration of Cl$^-$ in the original solution is higher than that in SSA due to the HgCl$_2$ added in the droplet.

In the global Hg cycling system, the reduction from Hg(II) to Hg(0) mainly occurs in two ways. (1) Hg(II) is reduced to Hg(I) by thermal reactions, such as BrHgO reacting with CO to produce HgBr and CO$_2$, and Hg(I)Br reacting with NO$_2$ to produce Hg(0) and BrNO$_2$.[90,91] (2) Reduction from Hg(II) to Hg(0) takes place largely through photolysis of Hg(II) on atmospheric surface, *e.g.*, aerosol's surface, air/gas interface.[92–96] The droplets and aerosol particles in air contribute the most reduction surface for Hg(II) to be adsorbed. The photoreduction of Hg(II) on the atmospheric surface has been recognized as the important source of Hg(0) production in air.[92] However, most of these gaseous-phase reduction reactions are only known from computations and have not been validated experimentally. Most surface-based photoreduction reactions have only been studied empirically and lack a solid mechanistic basis. Most Hg(II) compounds have been identified in urban and indoor air as HgBr$_2$ and HgCl$_2$.[96] It has been reported that O$_3$ potentially reduces HgCl$_2$ to Hg(0) under UV or solar radiation. Tong *et al.* demonstrated that O$_3$ can significantly promote the photolysis rate for HgCl$_2$ in the presence of UV radiation and speculated that atomic O, which results from the photodissociation of O$_3$ *via* solar radiation in the atmosphere, might reduce Hg(II)Cl$_2$ into Hg(I)Cl radicals.[55] Lyman *et al.* proposed that O$_3$ may react with HgCl$_2$ directly in air: HgCl$_2$ + 2O$_3$ → HgO + 2O$_2$ + 2ClO.[97] Ai *et al.* conducted an experiment to optically trap a single-particle reactor, which is made by mixing carbon nanotubes and mercury halogens in an ozone environment. They hypothesized that the Hg(II) could be reduced on the surface of the carbon nanotubes by O(^{3}p) photolyzed by O$_3$.[98] HgCl$_2$ can be photolyzed through the UVC radiation at 185 nm. However, in this experiment, no Raman band changes related to Hg(II) are observed when the surrounding RH is high. We speculate that is because the photolysis of Hg(II) is slower than its oxidation, and most reduced products of Hg(I) have been oxidized and returned to Hg(II).[99] If so, a small amount of Hg(I) in the suspended droplet would have been produced and balanced with Hg(II) *via* the photo-reduction and photo-oxidation reactions. On the other hand, as the ClO$_3^-$ is formed and Hg(I)ClO$_3$ is dissolvable in water, the Hg(I) can be in the free Hg$^+$ state in the aqueous system. As the Raman spectrum is based on vibrational frequencies of molecular bonds, it is unable to detect Hg(I) in its ionic state, other techniques may be used to confirm the above speculation.

As the Raman spectrum in Fig. 7 shows, the Hg–Cl band located at 314 cm^{-1} is observed after the droplets are stably trapped in a dry environment of RH condition below 41% ± 11%, and this means that instead of free Cl$^-$ in the aqueous system, more ionic Cl bonds with Hg(II) to form HgCl$_2$ molecules. Fig. 8a shows a contour plot of the Raman spectral intensity distribution of the SSA that contains Hg(II) as the droplet is trapped in air with the RH of 42%. Two locations were marked, where S is the position on the surface, and C is the position at the center of the trapped droplet. The corresponding Raman spectra of these two locations are shown in the insets in Fig. 8a. Compared with the Raman spectra in position S, the spectra in position C show one more band at 267 cm^{-1}, which is from HgCl$_4^{2-}$.[100] Instead of directly forming HgCl$_2$ inside the suspended aerosol particle, more Cl$^-$ bonds to HgCl$_2$ to form HgCl$_4^{2-}$. This is attributed to the photoreduction of Hg(II). As discussed in the previous paragraph, when the droplets are suspended under the high RH condition, a small amount of Hg(I) in the suspended droplet can be produced and balanced with Hg(II) *via* the photo-reduction and photo-oxidation reactions. The Hg(I) is also produced in lower RH conditions as the droplet is trapped under UVC radiation. As only one ionic Cl bonds to each Hg(I), more free Cl$^-$ is left in the aqueous system where it bonds with HgCl$_2$ to form HgCl$_4^{2-}$.

Fig. 8b shows the time-resolved Raman spectra of a SSA containing Hg(II) trapped under UVC radiation with a RH of 42%. As more free ionic Cl binds to HgCl$_2$ to form HgCl$_4^{2-}$, a new band at 267 cm^{-1} appears and increases in strength. After the droplet was exposed to UVC radiation for several minutes, another new band located at 166 cm^{-1} appears. This band is from Hg$_2$Cl$_2$.[101] The formation of Hg$_2$Cl$_2$ indicates that Hg(II) was reduced to Hg(I). After the Raman band of Hg$_2$Cl$_2$ appears, the trapped droplet becomes unstable and exits the trap in the next several seconds. This is because of the low dissolvability of Hg$_2$Cl$_2$ in water and the efflorescence of the suspended droplet. A small amount of Hg$_2$Cl$_2$ is crystallized inside of the SSA. The formation of solid particles affects the stability of the trapping.

In our exploration, the band change shown in Fig. 8b is difficult to observe. To observe the formation of Hg$_2$Cl$_2$, the RH is critical and must be in a specific range of 40–44%. This is because the droplets need to be sufficiently large to provide enough force to hold the solid Hg$_2$Cl$_2$. The interrogation time must be sufficiently long to capture the weak Raman signal. Meanwhile, the Hg$_2$Cl$_2$ that forms need to accumulate to a large volume for observation. For example, if the RH is too low due to the efflorescence of the droplets, the droplet's size will be too small to hold the Hg$_2$Cl$_2$ that crystallizes inside the droplets. If the RH is too high, the Cl$^-$ will be oxidized to ClO$_3^-$ in the aqueous system.

Nevertheless, based on the results, we hypothesized that under the UVC radiation of 185 nm and 254 nm, a small amount of Hg(II) is photolyzed to Hg(I), and the process reaches a balance between the photo-oxidation and photo-reduction in the SSA when the surrounding RH is high. As RH decreases, the SSA undergoes dehumidification, potentially leading to the formation and subsequent crystallization of Hg$_2$Cl$_2$.

© 2024 The Author(s). Published by the Royal Society of Chemistry

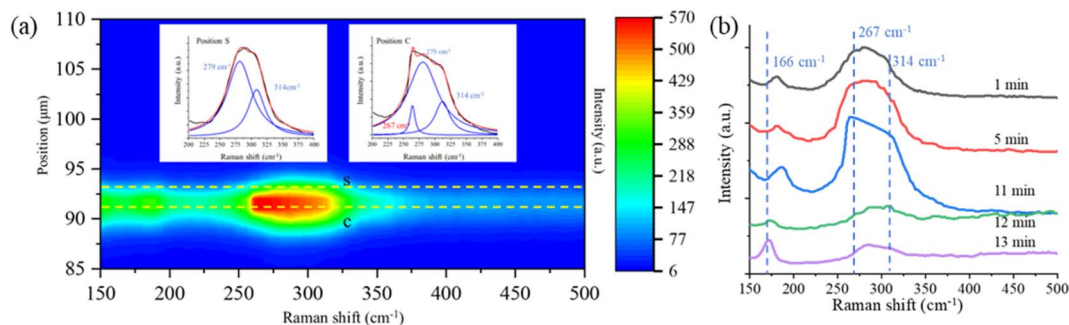*Environ. Sci.: Atmos.*, 2024, **4**, 911–924 | **919**

Fig. 8 (a) A contour plot of the spectral intensity distribution of Raman spectra of a SSA containing Hg(II). Two locations are marked where S is on the surface, and C is at the center. The insets show the position-resolved Raman spectra from two marked locations. (b) Raman band variations shown by the time-resolved Raman spectra as the SSA containing Hg(II) exposed to UVC radiation with RH of 42%. The new emerging peak at 166 cm^{-1} corresponds to Hg_2Cl_2, which indicates the photo-reduction reaction.

4. Conclusion

In this study, we investigated the heterogeneous chemistry and photochemistry of single suspended SSA particles and SSAs containing Hg(II) under different RH, ozone concentration, and UVC radiation using OT-RS.

In Part I, we explored the hygroscopicity, heterogeneous chemical reaction with O_3, and photochemical reaction with UVC radiation of single, suspended SSA particles by analyzing their Raman spectra. In this part, we show the RH-dependent single-particle Raman spectra of the SSA when it is suspended in air. Different spectral features show different sizes and states of the droplets. Specifically, the Raman signal is with no/weak OH-stretching band when it is trapped with RH below the ERH of 39% ± 8%. The solute of NaCl will neither be crystalline nor ionic, but NaCl molecules in the aqueous system. The droplet's size is smaller than 2 μm. The Raman spectra show a strong OH-stretching band under the RH condition of 39–69%. The solute of NaCl in SSA is in the ionic state, and the droplet's size is in the range of 4 to 20 μm, which are shown in the intensity of the Raman spectra. As the RH increases above 69% ± 5%, the WGM is observed in the Raman spectra. We also observe the heterogeneous chemical reaction between O_3 and a suspended single SSA particle, and the main reaction product is ClO_3^-. This reaction is supposed to happen only on the surface of the droplets when the environmental RH is higher than the ERH of SSA which is 39% ± 8%. Note that this reaction should be very slow in the natural environment because of the low ozone concentration. When the SSA is exposed to UVC radiation, the ionic Cl is oxidized to ClO_3^-, and a small amount of ClO_3^- can be further oxidized to ClO_4^- on the surface of the droplets. In the dry environment, the solute in SSA becomes supersaturated, and becomes NaCl molecules in the trapped SSA particle. Under this condition, no reaction is observed as the SSA is trapped under the UVC radiation.

In Part II, we explored the heterogeneous chemical reaction of the single suspended SSA particle containing Hg(II) with O_3, and the photochemical reaction of Hg(II) in SSA with UVC radiation. In this part, we show that the Raman signal response is similar to pure SSA particle when the SSA containing Hg(II) is trapped in air with different RH. When the solute inside the trapped droplet becomes supersaturated with the RH lower than the ERH of SSA containing Hg(II) of 41% ± 11%, the Raman band of $HgCl_2$ is observed. However, the size and state changes of SSAs containing Hg(II) are the same as the pure SSA particles. This indicates that the hygroscopicity of SSAs is not affected by the Hg(II). Furthermore, no reduction reaction of Hg(II) to Hg(I) is observed when the SSA containing Hg(II) is exposed to UVC radiation in the high RH condition. This is likely due to the photolysis process of Hg(II) being slower than its oxidation reaction. A small amount of Hg(I) may be produced, but in the free Hg^+ state, and it cannot be detected by Raman spectroscopy. With the RH of 40–44%, we observe the Raman band at 166 cm^{-1}, which indicates the formation of Hg_2Cl_2, as the droplet trapped under UVC radiation. Based on these results, the photo-reduction of Hg(II) to Hg(I) is hypothesized to happen in the SSA under UVC of 185 nm and 254 nm radiation. Limited quantities of Hg(I) are produced and balanced with Hg(II) between photo-oxidation and photo-reduction under high RH conditions. With the decrease of RH, the SSA experiences efflorescence, and the Hg_2Cl_2 is formed and crystallized inside the SSA.

Conflicts of interest

There are no conflicts to declare.

Acknowledgements

References

1 P. K. Quinn, D. B. Collins, V. H. Grassian, K. A. Prather and T. S. Bates, Chemistry and related properties of freshly emitted sea spray aerosol, *Chem. Rev.*, 2015, **115**(10), 4383–4399.

2 R. E. Cochran, O. S. Ryder, V. H. Grassian and K. A. Prather, Sea spray aerosol: The chemical link between the oceans,

atmosphere, and climate, *Acc. Chem. Res.*, 2015, **50**(3), 599–604.

3 J. Soares, M. Sofiev, C. Geels, J. H. Christensen, C. Andersson, S. Tsyro and J. Langner, Impact of climate change on the production and transport of sea salt aerosol on European seas, *Atmos. Chem. Phys.*, 2016, **16**(20), 13081–13104.

4 M. Tang, C. K. Chan, Y. J. Li, H. Su, Q. Ma, Z. Wu, G. Zhang, Z. Wang, M. Ge, M. Hu, H. He and X. Wang, A review of experimental techniques for aerosol hygroscopicity studies, *Atmos. Chem. Phys.*, 2019, **9**(19), 12631–12686.

5 O. Reich, M. J. Gleichweit, G. David, N. Leemann and R. Signorell, Hygroscopic growth of single atmospheric sea salt aerosol particles from mass measurement in an optical trap, *Environ. Sci.: Atmos.*, 2023, **3**(4), 695–707.

6 J. S. Walker, J. B. Wills, J. P. Reid, L. Wang, D. O. Topping, J. R. Butler and Y. H. Zhang, Direct comparison of the hygroscopic properties of ammonium sulfate and sodium chloride aerosol at relative humidities approaching saturation, *J. Phys. Chem. A*, 2010, **114**(48), 12682–12691.

7 M. N. Chan and C. K. Chan, Mass transfer effects in hygroscopic measurements of aerosol particles, *Atmos. Chem. Phys.*, 2005, **5**(10), 2703–2712.

8 J. F. Davies, A. E. Haddrell, A. M. J. Rickards and J. P. Reid, Simultaneous analysis of the equilibrium hygroscopicity and water transport kinetics of liquid aerosol, *Anal. Chem.*, 2013, **85**, 5819–5826.

9 G. Rovelli, R. E. H. Miles, J. P. Reid and S. L. Clegg, Accurate measurements of aerosol hygroscopic growth over a wide range in relative humidity, *J. Phys. Chem. A*, 2016, **120**, 4376–4388.

10 J. F. Davies, A. E. Haddrell and J. P. Reid, Time-resolved measurements of the evaporation of volatile components from single aerosol droplets, *Aerosol Sci. Technol.*, 2012, **46**, 666–677.

11 A. Peckhaus, A. Kiselev, R. Wagner, D. Duft and T. Leisner, Temperature-dependent formation of NaCl dihydrate in levitated NaCl and sea salt aerosol particles, *J. Chem. Phys.*, 2016, **145**(24), 244503.

12 P. R. Tumminello, R. C. James, S. Kruse, A. Kawasaki, A. Cooper, I. Guadalupe-Diaz, K. L. Zepeda, D. R. Crocker, K. J. Mayer, J. S. Sauer, C. Lee, K. A. Prather and J. H. Slade, Evolution of sea spray aerosol particle phase state across a phytoplankton bloom, *ACS Earth Space Chem.*, 2021, **5**(11), 2995–3007.

13 J. F. Davies, A. E. Haddrell, R. E. H. Miles, C. R. Bull and J. P. Reid, Bulk, surface, and gas-phase limited water transport in aerosol, *J. Phys. Chem. A*, 2012, **116**, 10987–10998.

14 E. Vignati, M. C. Facchini, M. Rinaldi, C. Scannell, D. Ceburnis, J. Sciare, M. Kanakidou, S. Myriokefalitakis, F. Dentener and C. D. O'Dowd, Global scale emission and distribution of sea-spray aerosol: Sea-salt and organic enrichment, *Atmos. Environ.*, 2010, **44**(5), 670–677.

15 A. P. Ault, R. C. Moffet, J. Baltrusaitis, D. B. Collins, M. J. Ruppel, L. A. Cuadra-Rodriguez, D. Zhao, T. L. Guasco, C. J. Ebben, F. M. Geiger, T. H. Bertram, K. A. Prather and V. H. Grassian, Size-dependent changes in sea spray aerosol composition and properties with different seawater conditions, *Environ. Sci. Technol.*, 2013, **47**(11), 5603–5612.

16 T. H. Bertram, R. E. Cochran, V. H. Grassian and E. A. Stone, Sea spray aerosol chemical composition: elemental and molecular mimics for laboratory studies of heterogeneous and multiphase reactions, *Chem. Soc. Rev.*, 2018, **47**(7), 2374–2400.

17 B. Su, T. Wang, G. Zhang, Y. Liang, C. Lv, Y. Hu, L. Li, Z. Zhou, X. Wang and X. Bi, A review of atmospheric aging of sea spray aerosols: Potential factors affecting chloride depletion, *Atmos. Environ.*, 2022, **290**, 119365.

18 E. Athanasopoulou, M. Tombrou, S. N. Pandis and A. G. Russell, The role of sea-salt emissions and heterogeneous chemistry in the air quality of polluted coastal areas, *Atmos. Chem. Phys.*, 2018, **8**(19), 5755–5769.

19 M. M. van Herpen, Q. Li, A. Saiz-Lopez, J. B. Liisberg, T. Röckmann, C. A. Cuevas, R. P. Fernandez, J. E. Mak, N. M. Mahowald, P. Hess, D. Meidan, J. W. Stuut and M. S. Johnson, Photocatalytic chlorine atom production on mineral dust–sea spray aerosols over the North Atlantic, *Proc. Natl. Acad. Sci. U. S. A.*, 2023, **120**(31), e2303974120.

20 I. N. Tang, A. C. Tridico and K. H. Fung, Thermodynamic and optical properties of sea salt aerosols, *J. Geophys. Res.: Atmos.*, 1997, **102**(D19), 23269–23275.

21 P. J. Gallimore, P. Achakulwisut, F. D. Pope, J. F. Davies, D. R. Spring and M. Kalberer, Importance of relative humidity in the oxidative ageing of organic aerosols: case study of the ozonolysis of maleic acid aerosol, *Atmos. Chem. Phys.*, 2011, **11**, 12181–12195.

22 A. E. Haddrell, J. F. Davies, R. E. H. Miles, J. P. Reid, L. A. Dailey and D. Murnane, Dynamics of aerosol size during inhalation: Hygroscopic growth of commercial nebulizer formulations, *Int. J. Pharm.*, 2014, **463**, 50–61.

23 X. Li, D. Gupta, H. Eom, H. Kim and C.-U. Ro, Deliquescence and efflorescence behavior of individual NaCl and KCl mixture aerosol particles, *Atmos. Environ.*, 2014, **82**, 36–43.

24 D. Gupta, H. Kim, G. Park, X. Li, H.-J. Eom and C.-U. Ro, Hygroscopic properties of NaCl and NaNO$_3$ mixture particles as reacted inorganic sea-salt aerosol surrogates, *Atmos. Chem. Phys.*, 2015, **15**, 3379–3393.

25 G. Biskos, A. Malinowski, L. M. Russell, P. R. Buseck and S. T. Martin, Nanosize effect on the deliquescence and the efflorescence of sodium chloride particles, *Aerosol Sci. Technol.*, 2006, **40**, 97–106.

26 D. Gupta, H.-J. Eom, H.-R. Cho and C.-U. Ro, Hygroscopic behavior of NaCl–MgCl$_2$ mixture particles as nascent sea-spray aerosol surrogates and observation of efflorescence during humidification, *Atmos. Chem. Phys.*, 2015, **15**, 11273–11290.

27 A. E. Haddrell, J. F. Davies and J. P. Reid, Dynamics of particle size on inhalation of environmental aerosol and impact on deposition fraction, *Environ. Sci. Technol.*, 2015, **49**, 14512–14521.

© 2024 The Author(s). Published by the Royal Society of Chemistry

Environ. Sci.: Atmos., 2024, **4**, 911–924 | **921**

28 H.-J. Tong, J. P. Reid, D. L. Bones, B. P. Luo and U. K. Krieger, Measurements of the timescales for the mass transfer of water in glassy aerosol at low relative humidity and ambient temperature, *Atmos. Chem. Phys.*, 2011, **11**, 4739–4754.

29 P. Zieger, R. Fierz-Schmidhauser, E. Weingartner and U. Baltensperger, Effects of relative humidity on aerosol light scattering: results from different European sites, *Atmos. Chem. Phys.*, 2013, **13**, 10609–10631.

30 P. Zieger, R. Fierz-Schmidhauser, M. Gysel, J. Strom, S. Henne, K. E. Yttri, U. Baltensperger and E. Weingartner, Effects of relative humidity on aerosol light scattering in the Arctic, *Atmos. Chem. Phys.*, 2010, **10**, 3875–3890.

31 M. I. Cotterell, R. E. Willoughby, B. R. Bzdek, A. J. Orr-Ewing and J. P. Reid, A complete parameterisation of the relative humidity and wavelength dependence of the refractive index of hygroscopic inorganic aerosol particles, *Atmos. Chem. Phys.*, 2017, **17**, 9837–9851.

32 J. Gao, Y. Wei, G. Shi, H. Yu, Z. Zhang, S. Song, W. Wang, D. Liang and Y. Feng, Roles of RH, aerosol pH and sources in concentrations of secondary inorganic aerosols, during different pollution periods, *Atmos. Environ.*, 2020, **241**, 117770.

33 B. R. Bzdek and M. V. Johnston, New particle formation and growth in the troposphere, *Anal. Chem.*, 2010, **82**, 7871–7878.

34 K. Yu, C. Lin, S. Yang and P. Zhao, Enhancement effect of relative humidity on the formation and regional respiratory deposition of secondary organic aerosol, *J. Hazard. Mater.*, 2011, **191**, 94–102.

35 W. Hu, B. B. Palm, D. A. Day, P. Campuzano-Jost, J. E. Krechmer, Z. Peng, S. S. de Sá, S. T. Martin, M. L. Alexander, K. Baumann, L. Hacker, A. Kiendler-Scharr, A. R. Koss, J. A. de Gouw, A. H. Goldstein, R. Seco, S. J. Sjostedt, J.-H. Park, A. B. Guenther, S. Kim, F. Canonaco, A. S. H. Prévôt, W. H. Brune and J. L. Jimenez, Volatility and lifetime against OH heterogeneous reaction of ambient isoprene-epoxydiols-derived secondary organic aerosol (IEPOX-SOA), *Atmos. Chem. Phys.*, 2016, **16**, 11563–11580.

36 Z. Li, K. A. Smith and C. D. Cappa, Influence of relative humidity on the heterogeneous oxidation of secondary organic aerosol, *Atmos. Chem. Phys.*, 2018, **18**, 14585–14608.

37 P. J. Gallimore, P. Achakulwisut, F. D. Pope, J. F. Davies, D. R. Spring and M. Kalberer, Importance of relative humidity in the oxidative ageing of organic aerosols: case study of the ozonolysis of maleic acid aerosol, *Atmos. Chem. Phys.*, 2011, **11**, 12181–12195.

38 N. Kang, W. A. Jackson, P. K. Dasgupta and T. A. Anderson, Perchlorate production by ozone oxidation of chloride in aqueous and dry systems, *Sci. Total Environ.*, 2008, **405**(1–3), 301–309.

39 N. Kang, T. A. Anderson, B. Rao and W. A. Jackson, Characteristics of perchlorate formation via photodissociation of aqueous chlorite, *Environ. Chem.*, 2009, **6**(1), 53–59.

40 H. Cosson and W. R. Ernst, Photodecomposition of chlorine dioxide and sodium chlorite in aqueous solution by irradiation with ultraviolet light, *Ind. Eng. Chem. Res.*, 1994, **33**(6), 1468–1475.

41 L. R. B. Yeatts and H. Taube, The kinetics of the reaction of ozone and chloride ion in acid aqueous solution, *J. Am. Chem. Soc.*, 1949, **71**(12), 4100–4105.

42 N. Kang, T. A. Anderson and W. A. Jackson, Photochemical formation of perchlorate from aqueous oxychlorine anions, *Anal. Chim. Acta*, 2006, **567**(1), 48–56.

43 J. H. Johansson, M. E. Salter, J. A. Navarro, C. Leck, E. D. Nilsson and I. T. Cousins, Global transport of perfluoroalkyl acids via sea spray aerosol, *Environ. Sci.: Processes Impacts*, 2019, **21**(4), 635–649.

44 R. P. Mason and G. R. Sheu, Role of the ocean in the global mercury cycle, *Global Biogeochem. Cycles*, 2002, **16**(4), 1093.

45 E. M. Sunderland and R. P. Mason, Human impacts on open ocean mercury concentrations, *Global Biogeochem. Cycles*, 2007, **21**(4), GB4022.

46 N. Batrakova, O. Travnikov and O. Rozovskaya, Chemical and physical transformations of mercury in the ocean: a review, *OS*, 2014, **10**(6), 1047–1063.

47 B. Gworek, O. Bemowska-Kałabun, M. Kijeńska and J. Wrzosek-Jakubowska, Mercury in marine and oceanic waters—a review, *Water, Air, Soil Pollut.*, 2016, **227**(10), 371.

48 C. D. Holmes, D. J. Jacob, R. P. Mason and D. A. Jaffe, Sources and deposition of reactive gaseous mercury in the marine atmosphere, *Atmos. Environ.*, 2009, **43**(14), 2278–2285.

49 E. G. Malcolm, A. C. Ford, T. A. Redding, M. C. Richardson, B. M. Strain and S. W. Tetzner, Experimental investigation of the scavenging of gaseous mercury by sea salt aerosol, *J. Atmos. Chem.*, 2009, **63**(3), 221–234.

50 M. S. Gustin, S. M. Dunham-Cheatham, J. Huang, S. Lindberg and S. N. Lyman, Development of an understanding of reactive mercury in ambient air: a review, *Atm*, 2021, **12**(1), 73.

51 L. Si and P. A. Ariya, Recent advances in atmospheric chemistry of mercury, *Atm*, 2018, **9**(2), 76.

52 E. G. Malcolm, G. J. Keeler and M. S. Landis, The effects of the coastal environment on the atmospheric mercury cycle, *J. Geophys. Res.: Atmos.*, 2003, **108**(D12), 4357.

53 A. Saiz-Lopez, S. P. Sitkiewicz, D. Roca-Sanjuán, J. M. Oliva-Enrich, J. Z. Dávalos, R. Notario, M. Jiskra, Y. Xu, F. Wang, C. P. Thackray, E. M. Sunderland, D. J. Jacob, O. Travnikov, C. A. Cuevas, A. U. Acuña, D. Rivero, J. M. C. Plane, D. E. Kinnison and J. E. Sonke, Photoreduction of gaseous oxidized mercury changes global atmospheric mercury speciation, transport and deposition, *Nat. Commun.*, 2018, **9**(1), 4796.

54 H. M. Hannah, D. J. Jacob, Y. Zhang, T. S. Dibble, F. Slemr, H. M. Amos, J. A. Schmidt, E. S. Corbitt, E. A. Marais and E. M. Sunderland, A new mechanism for atmospheric mercury redox chemistry: implications for the global mercury budget, *Atmos. Chem. Phys.*, 2017, **17**(10), 6353–6371.

55 Y. Tong, H. Zhang, H. Lin, B. de Foy, L. Chen, W. Zhang, X. Wang and C. Guan, A potential route for photolytic reduction of HgCl$_2$ and HgBr$_2$ in dry air and analysis about the impacts from Ozone, *Atmos. Res.*, 2021, **249**, 105310.

56 I. M. Hedgecock and N. Pirrone, Mercury and photochemistry in the marine boundary layer-modelling studies suggest the in situ production of reactive gas phase mercury, *Atmos. Environ.*, 2001, **35**(17), 3055–3062.

57 H. Luo, Q. Cheng and X. Pan, Photochemical behaviors of mercury (Hg) species in aquatic systems: A systematic review on reaction process, mechanism, and influencing factor, *Sci. Total Environ.*, 2020, **720**, 137540.

58 A. Qureshi, N. J. O'Driscoll, M. MacLeod, Y. M. Neuhold and K. Hungerbühler, Photoreactions of mercury in surface ocean water: gross reaction kinetics and possible pathways, *Environ. Sci. Technol.*, 2010, **44**(2), 644–649.

59 L. Whalin, E. H. Kim and R. Mason, Factors influencing the oxidation, reduction, methylation and demethylation of mercury species in coastal waters, *Mar. Chem.*, 2007, **107**(3), 278–294.

60 N. J. O'Driscoll, E. Vost, E. Mann, S. Klapstein, R. Tordon and M. Lukeman, Mercury photoreduction and photooxidation in lakes: effects of filtration and dissolved organic carbon concentration, *J. Environ. Sci.*, 2018, **68**, 151–159.

61 J. S. Sauer, K. J. Mayer, C. Lee, M. R. Alves, S. Amiri, C. J. Bahaveolos, E. B. Franklin, D. R. Crocker, D. Dang, J. Dinasquet, L. A. Garofalo, C. P. Kaluarachchi, D. B. Kilgour, L. E. Mael, B. A. Mitts, D. R. Moon, A. N. Moore, C. K. Morris, C. A. Mullenmeister, C.-M. Ni, M. A. Pendergraft, D. Petras, R. M. C. Simpson, S. Smith, P. R. Tumminello, J. L. Walker, P. J. DeMott, D. K. Farmer, A. H. Goldstein, V. H. Grassian, J. S. Jaffe, F. Malfatti, T. R. Martz, J. H. Slade, A. V. Tivanski, T. H. Bertram, C. D. Cappah and K. A. Prather, The Sea Spray Chemistry and Particle Evolution study (SeaSCAPE): overview and experimental methods, *Environ. Sci.: Processes Impacts*, 2022, **24**, 290.

62 T. H. Bertram, R. E. Cochran, V. H. Grassian and E. A. Stone, Sea spray aerosol chemical composition: elemental and molecular mimics for laboratory studies of heterogeneous and multiphase reactions, *Chem. Soc. Rev.*, 2018, **47**, 2374.

63 J. P. Patterson, D. B. Collins, J. M. Michaud, J. L. Axson, C. M. Sultana, T. Moser, A. C. Dommer, J. Conner, V. H. Grassian, M. D. Stokes, G. B. Deane, J. E. Evans, M. D. Burkart, K. A. Prather and N. C. Gianneschi, Sea spray aerosol structure and composition using cryogenic transmission electron microscopy, *ACS Cent. Sci.*, 2016, **2**, 40–47.

64 H. D. Lee, S. Wigley, C. Lee, V. W. Or, E. S. Hasenecz, E. A. Stone, V. H. Grassian, K. A. Prather and A. V. Tivanski, Physicochemical mixing state of sea spray aerosols: morphologies exhibit size dependence, *ACS Earth Space Chem.*, 2020, **4**, 1604–1611.

65 S. R. Schneider, D. B. Collins, C. Y. Lim, L. Zhu and J. P. D. Abbatt, Formation of secondary organic aerosol from the heterogeneous oxidation by ozone of a phytoplankton culture, *ACS Earth Space Chem.*, 2019, **3**, 2298–2306.

66 J. V. Trueblood, X. Wang, V. W. Or, M. R. Alves, M. V. Santander, K. A. Prather and V. H. Grassian, The old and the new: Aging of sea spray aerosol and formation of secondary marine aerosol through OH oxidation reactions, *ACS Earth Space Chem.*, 2019, **3**, 2307–2314.

67 K. J. Mayer, X. Wang, M. V. Santander, B. A. Mitts, J. S. Sauer, C. M. Sultana, C. D. Cappa and K. A. Prather, Secondary marine aerosol plays a dominant role over primary sea spray aerosol in cloud formation, *ACS Cent. Sci.*, 2020, **6**, 2259–2266.

68 Y. Ai, C. Wang, Y. L. Pan and G. Videen, Characterization of single fungal aerosol particles in a reactive atmospheric environment using time-resolved optical trapping-Raman spectroscopy (OT-RS), *Environ. Sci.: Atmos.*, 2022, **2**(4), 591–600.

69 Y. Ai, H. Alali, Y. L. Pan, G. Videen and C. Wang, Single-particle optical-trapping Raman spectroscopy for the detection and identification of aerosolized airborne biological particles, *Meas. Sci. Technol.*, 2021, **32**(5), 055207.

70 H. Alali, Y. Ai, Y. L. Pan, G. Videen and C. Wang, A collection of molecular fingerprints of single aerosol particles in air for potential identification and detection using optical trapping-Raman spectroscopy, *Mol*, 2022, **27**(18), 5966.

71 A. Kalume, C. Wang, J. Santarpia and Y. L. Pan, Study of single airborne particle using laser-trapped submicron position-resolved temporal Raman spectroscopy, *Chem. Phys. Lett.*, 2018, **706**, 255–260.

72 J. B. Wills, K. J. Knox and J. P. Reid, Optical control and characterisation of aerosol, *Chem. Phys. Lett.*, 2009, **481**(4–6), 153–165.

73 M. J. Rossi, Heterogeneous reactions on salts, *Chem. Rev.*, 2003, **103**(12), 4823–4882.

74 B. J. Finlayson-Pitts, The tropospheric chemistry of sea salt: A molecular-level view of the chemistry of NaCl and NaBr, *Chem. Rev.*, 2003, **103**(12), 4801–4822.

75 E. M. Knipping and D. Dabdub, Modeling Cl$_2$ formation from aqueous NaCl particles: Evidence for interfacial reactions and importance of Cl$_2$ decomposition in alkaline solution, *J. Geophys. Res.: Atmos.*, 2002, **107**(D18), 8.

76 S. Roy and J. A. Mondal, Breaking" and "Making" of Water Structure at the Air/Water− Electrolyte (NaXO$_3$; X= Cl, Br, I) Interface, *J. Phys. Chem. Lett.*, 2021, **12**(7), 1955–1960.

77 L. Xu, G. Csekő, A. Petz and A. K. Horváth, Kinetics and mechanism of the oxidation of pentathionate ion by chlorine dioxide in a slightly acidic medium, *J. Phys. Chem. A*, 2014, **118**(8), 1293–1299.

78 Z. Wu, A. Wang and Z. Ling, Spectroscopic study of perchlorates and other oxygen chlorides in a Martian environmental chamber, *Earth Planet. Sci. Lett.*, 2016, **452**, 123–132.

79 W. Xi, B. K. Shrestha and A. J. Haes, Promoting intra-and intermolecular interactions in surface-enhanced Raman scattering, *Anal. Chem.*, 2017, **90**(1), 128–143.

© 2024 The Author(s). Published by the Royal Society of Chemistry

Environ. Sci.: Atmos., 2024, **4**, 911–924 | **923**

80 L. Rkiouak, M. J. Tang, J. C. J. Camp, J. McGregor, I. M. Watson, R. A. Cox, M. Kalberer, A. D. Ward and F. D. Pope, Optical trapping and Raman spectroscopy of solid particles, *Phys. Chem. Chem. Phys.*, 2014, **16**(23), 11426–11434.

81 B. Zachhuber, G. Ramer, A. Hobro, E. T. H. Chrysostom and B. Lendl, Stand-off Raman spectroscopy: a powerful technique for qualitative and quantitative analysis of inorganic and organic compounds including explosives, *Anal. Bioanal. Chem.*, 2011, **400**, 2439–2447.

82 H. H. Eysel, Raman intensities of liquids: absolute scattering activities and Cl-O bond EOPs of ClO^-, ClO_2^-, ClO_3^- and ClO_4^- ions in aqueous solution, *Spectrochim. Acta, Part A*, 1988, **44**(10), 991–997.

83 J. B. Bates, A. S. Quist and G. E. Boyd, Vibrational spectra of molten and aqueous $NaClO_3$ and $KClO_3$, *Chem. Phys. Lett.*, 1972, **16**(3), 473–476.

84 K. Takahashi, S. Hayashi and Y. Matsumi, Quantum yields of O(1D) formation in the photolysis of ozone between 230 and 308 nm, *J. Geophys. Res.*, 2002, **107**(D20), 4440.

85 H. Voraberger, V. Ribitsch, M. Janotta and B. Mizaikoff, Application of mid-infrared spectroscopy: measuring hydrogen peroxide concentrations in bleaching baths, *Appl. Spectrosc.*, 2003, **57**(5), 574–579.

86 K. Yoshihara, Y. Takatori, K. Miyazaki and Y. Kajii, Ultraviolet light-induced water-droplet formation from wet ambient air, *Proc. Jpn. Acad., Ser. B*, 2007, **83**, 320–325.

87 J. Du, Z. Liu, C. Bai, L. Li, Y. Zhao, L. Wang and J. Pan, Concentration distributions and reaction pathways of species in the mass transfer process from atmospheric pressure plasma jet to water, *Eur. Phys. J. D*, 2018, **72**, 1–7.

88 Y. Wang, W. Zhu, K. Lin, L. Yuan, X. Zhou and S. Liu, Ratiometric detection of Raman hydration shell spectra, *J. Raman Spectrosc.*, 2016, **47**(10), 1231–1238.

89 G. J. Janz and D. W. James, Vibrational spectra of molten halides of mercury. I. Mercuric chloride, mercuric bromide, and mercury chlorobromide, *J. Chem. Phys.*, 1963, **38**(4), 902–905.

90 Y. Jiao and T. S. Dibble, First kinetic study of the atmospherically important reactions $BrHg + NO_2$ and BrHg + HOO, *Phys. Chem. Chem. Phys.*, 2017, **19**(3), 1826–1838.

91 R. Wu, C. Wang and T. S. Dibble, First experimental kinetic study of the atmospherically important reaction of BrHg + NO_2, *Chem. Phys. Lett.*, 2020, **759**, 137928.

92 C. Deng, Y. Tong, L. Chen, W. Yuan, Y. Sun, J. Li, X. Wang, W. Zhang, H. Lin, H. Xie and X. Bu, Impact of particle chemical composition and water content on the photolytic reduction of particle-bound mercury, *Atmos. Environ.*, 2019, **200**, 24–33.

93 Y. Tong, T. Eichhorst, M. R. Olson, J. E. McGinnis, I. Turner, A. P. Rutter, M. M. Shafer, X. Wang and J. J. Schauer, Atmospheric photolytic reduction of Hg (II) in dry aerosols, *Environ. Sci.: Processes Impacts*, 2013, **15**(10), 1883–1888.

94 A. U. Lewandowska, M. Bełdowska, A. Witkowska, L. Falkowska and K. Wiśniewska, Mercury bonds with carbon (OC and EC) in small aerosols (PM1) in the urbanized coastal zone of the Gulf of Gdansk (southern Baltic), *Ecotoxicol. Environ. Saf.*, 2018, **157**, 350–357.

95 P. A. Ariya, M. Amyot, A. Dastoor, D. Deeds, A. Feinberg, G. Kos, A. Poulain, A. Ryjkov, K. Semeniuk, M. Subir and K. Toyota, Mercury physicochemical and biogeochemical transformation in the atmosphere and at atmospheric interfaces: A review and future directions, *Chem. Rev.*, 2015, **115**(10), 3760–3802.

96 V. Shah, D. J. Jacob, C. P. Thackray, X. Wang, E. M. Sunderland, T. S. Dibble, A. Saiz-Lopez, I. Černušák, V. Kellö, P. J. Castro, R. Wu and C. Wang, Improved mechanistic model of the atmospheric redox chemistry of mercury, *Environ. Sci. Technol.*, 2021, **55**(21), 14445–14456.

97 S. N. Lyman, D. A. Jaffe and M. S. Gustin, Release of mercury halides from KCl denuders in the presence of ozone, *Atmos. Chem. Phys.*, 2010, **10**(17), 8197–8204.

98 Y. Ai, C. Wang, G. Videen and Y. L. Pan, Optically levitated, single-particle reactor for the study of surface and heterogeneous chemistry-reactions of particulate-bound mercury with ozone in air, *Chem. Phys. Lett.*, 2023, **817**, 140428.

99 A. Saiz-Lopez, O. Travnikov, J. E. Sonke, C. P. Thackray, D. J. Jacob, J. Carmona-García, A. Francés-Monerris, D. Roca-Sanjuán, A. U. Acuña, J. Z. Dávalos, C. A. Cuevas, M. Jiskra, F. Wang, J. Bieser, J. M. C. Plane and J. S. Francisco, Photochemistry of oxidized Hg (I) and Hg (II) species suggests missing mercury oxidation in the troposphere, *Proc. Natl. Acad. Sci. U. S. A.*, 2020, **117**(49), 30949–30956.

100 P. B. Bentham, C. G. Romak and H. F. Shurvell, A Raman spectroscopic study of the equilibria in aqueous solutions of Hg (II) chloride, *Can. J. Chem.*, 1985, **63**(8), 2303–2307.

101 G. A. Voyiatzis and G. N. Papatheodorou, Raman spectroscopic studies of metal-metal halide molten mixtures: the mercury-mercury (II) halide systems, *Inorg. Chem.*, 1992, **31**(10), 1945–1951.